



PERGAMON

Available online at www.sciencedirect.com

SCIENCE @ DIRECT®

Planetary and Space Science 51 (2003) 353–364

Planetary
and
Space Science

www.elsevier.com/locate/pss

Cassini RADAR: prospects for Titan surface investigations using the microwave radiometer

Ralph D. Lorenz^{a,*}, Gilles Biolluz^b, Pierre Encrenaz^b, Michael A. Janssen^c,
Richard D. West^c, Duane O. Muhleman^d

^aLunar and Planetary Laboratory, University of Arizona, 1629 E. University Boulevard, Tucson, AZ 85721-0092, USA

^bDEMIRM, 61. Ave. de l'Observatoire, Paris 75014, France

^cJet Propulsion Laboratory, California Institute of Technology, 4800 Oak Grove Drive, Pasadena, CA 91109, USA

^dDepartment of Geological and Planetary Science, California Institute of Technology, Pasadena, CA 91125, USA

Received 25 June 2001; received in revised form 23 August 2002; accepted 4 October 2002

Abstract

The Radar instrument on the Cassini spacecraft can be used in a passive radiometric mode to map the microwave emission from Titan: these will be the first resolved microwave emission measurements of an icy satellite. Observation plans and the theory for their interpretation is presented: these data should be able to provide crude composition maps of Titan's surface, confirm equator-to-pole temperature gradients without the influence of the atmospheric effects which affect infrared observations and place constraints on surface and subsurface temperature variations. Additionally, passive radiometry will also provide some bistatic reflection measurements, using the sun as a source, which may be used to constrain roughness of ethane seas.

© 2003 Elsevier Science Ltd. All rights reserved.

Keywords: Microwave; Radiometry; Remote sensing; Titan

1. Introduction

Although microwave remote sensing is most often associated with active sensing by Radar, passive measurements can provide important information. Microwave radiometry and spectroscopy is widely used in the study of planetary atmospheres (e.g. Janssen, 1993) and on Earth, passive microwave radiometers (e.g. Skou, 1989) are routinely used to monitor snow and ice cover, in forestry and to determine soil moisture content and sea surface salinity and wind-speed. Passive radiometry is a powerful complement to radar backscatter measurement, especially in the case of a liquid surface when measurements in orthogonal polarizations can be made.

Microwave radiometry has been used to investigate Venus surface properties (e.g. Pettengill et al., 1992; Johnson and Baker, 1994), and to determine a density from the anomalously high-emissivity 'Stealth' region on Mars (Ivanov, 1998).

A microwave radiometer was carried on the first successful interplanetary probe, Mariner 2, to Venus in 1962. Cassini continues the rich tradition of passive microwave sensing with the incorporation of a radiometer in the RADAR instrument designed to study the surface of Saturn's moon Titan. No outer planets mission has yet carried such a microwave instrument, and in this paper we explore some of the insights such sensing may offer about Titan. (NB while radar as a technique is a widely used term, although originally an abbreviation, we refer to the Cassini instrument specifically as all upper case.)

2. Cassini RADAR instrument and observation scenario

2.1. The Cassini RADAR

The Cassini RADAR instrument is a multimode microwave instrument that uses the 4 m high gain antenna (HGA) on Cassini. The instrument operates at Ku band (13.78 GHz, or 2.2 cm wavelength) and is described in some detail in Elachi et al. (in press). Other relevant papers are an early description (Elachi et al., 1991) and simulation

* Corresponding author. Tel.: +1-520-621-5585; fax: +1-520-621-4933.

E-mail address: rlorenz@lpl.arizona.edu (R.D. Lorenz).

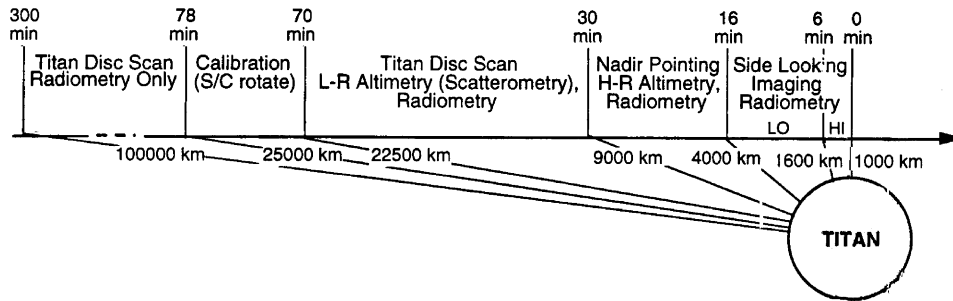


Fig. 1. Timeline of a radar-dedicated encounter, marked with times before closest approach. Radiometry takes place throughout, and is the only mode for distant observations. After 0 min the sequence repeats in reverse.

work on backscatter and imaging (Melacci et al., 1998). The RADAR's prime operating mode is as a synthetic aperture radar (SAR) mapper during Titan close approaches. Here it uses five beams, arranged in a line orthogonal to the spacecraft groundtrack, to build a long swath of backscatter imagery around 200 km across.

The instrument can also be operated as an altimeter, with the main beam (Beam 3, a circular beam 0.35° across) pointed at nadir, and will measure elevations along the groundtrack with a vertical resolution of around 100 m and a horizontal footprint of 30 km or so. A low-resolution altimeter or scatterometric mode is also available, where a smaller bandwidth improves signal-to-noise at the expense of range resolution. This allows the backscatter of areas off-nadir to be measured, with lower spatial resolution but at longer ranges from Titan than are possible in the SAR mode. The long axes of the beams are aligned along the Y -axis of the Cassini spacecraft. The E -field sensed by the instrument is along the spacecraft X direction.

The instrument also measures the microwave radiation incident on it between echo pulses, and hence the microwave brightness of targets in the beam. These radiometric measurements can be performed entirely passively, as for example at long ranges (50,000–100,000 km) from Titan, or while active measurements are being taken in the other modes closer in.

Internal calibrations are made with a noise diode and a resistive load whose characteristics are known. Even with these calibrations alone, short-term variations in microwave brightness can be easily measured, as evidenced by the observations made during Cassini's Earth swingby in August 1999. This observation shows clearly sea-surface characteristics in the Pacific ocean, the transition to land, and the low temperature of the Andes mountains (Lorenz et al., 2001a). Ideally, cold space would be observed during a radiometry sequence to establish the zero level and hence assign an absolutely calibrated brightness temperature to subsequent targets. Such cold-space observations, not permitted during the Earth swingby, will be made wherever possible during Cassini's Saturn tour.

The instrument was also operated during the Cassini flyby of Jupiter. There, with cold-sky calibrations and bet-

ter instrument performance models (e.g. knowing the beam pattern accurately after cruise observations of calibration sources like the sun) it was able to resolve synchrotron emission with a detection limit of only a few tenths of a K, even though such emission would be adjacent to Jupiter itself, whose thermal emission temperature is around 170 K (Bolton et al., 2002). At Saturn, under good conditions, the instrument is expected to provide absolute brightness temperatures good to around 2 K, and short-term variations (depending on integration time) of around 0.1 K.

2.2. Titan encounter scenario

Cassini will make around 44 Titan encounters during its nominal mission. A typical encounter (Fig. 1) is at 6 km s^{-1} with a closest approach distance of 1000–2500 km. RADAR observations will not be made at all flybys, since some will be devoted to optical remote sensing (ORS—these instruments are mounted orthogonally to the Z -axis along which the RADAR beam is oriented), and others are devoted to radio science, where the HGA is oriented towards the Earth for doppler tracking for gravity field measurements (or towards the Earth's refracted radio image for radio occultation measurements of the atmosphere).

On a RADAR-dedicated flyby, observations would begin several hours before closest approach, at a range of around 100,000 km. After a warm-up period to stabilise the noise diode reference and cold-sky measurements, the beam would be pointed at Titan. At a range of 100,000 km, the beam footprint is around 500 km across (a resolution of 1/10th of Titan's disk, or a little poorer than present-day optical imaging of Titan by groundbased speckle and adaptive optics techniques in the near-infrared and by HST). The beam will be moved in a spiral or raster pattern to cover the whole disk. Various coning rates and strategies are possible (e.g. see Fig. 2): an important element in the observing strategy is to control the polarization of the beam.

Since the radiometer is linearly polarized, rotating the spacecraft at the same rate as a spiral scan can allow the polarization vector to be always radial to the target—thus

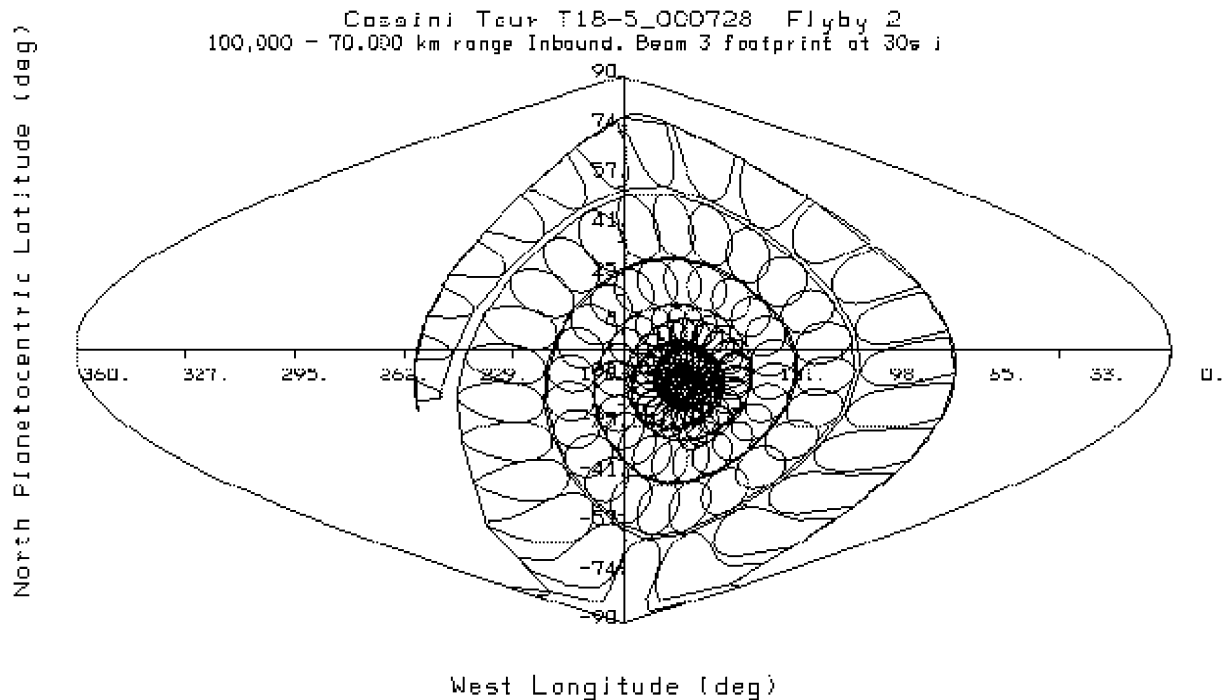


Fig. 2. Sinusoidal projection of a simulated spiral scan at some distance from Titan. The beam footprint diameter is of course proportional to distance—this spiral is inward during approach. The beam flux is measured many times per second, but footprints are shown here only every half minute. The spiral rate will be limited by the spacecraft attitude control system: by rotating the whole spacecraft about the Z-axis, the polarization vector can be selected.

the vertically polarized radiance of the target is sensed. On the other hand, an orientation that is circumferential to the spiral would force the polarization to be horizontal. Another approach would be to perform a mosaic or spiral in one polarization (e.g. with the axis along the pole vector of Titan) rotate the spacecraft and repeat in two other orientations to solve for the horizontally and vertically polarized emissions.

The optimum suite of observations for a given observation period have not yet been determined, since the choice of spiral rate or mosaic-type depends in part on spacecraft turn rate and sun constraint considerations which have not yet been modeled in the Cassini pointing design tool (PDT) for all flybys. Sufficiently rapid scanning may allow multiple looks (polarizations and incidence angles) at each point from a single flyby. The root mean square temperature error for 1 s of integration is 0.025 K, so signal-to-noise is not a significant limitation—spacecraft turn rates are the limiting factor. For the early encounters presently being planned, the strategy adopted is a set of rasters (since a square raster obtains cold-sky calibrations on every leg, to maximize the radiometric precision of the measurement) at 3 polarizations rotated by 60° covering most of Titan's disk.

Within 25,000 km range (about 1 h before closest approach) active scatterometer measurements become possible, and the RADAR may be operated actively. Radiometer observations can of course continue, although the incidence angles, etc. may be optimized for scatterometry, rather than the ridealong radiometry (see Fig. 3).

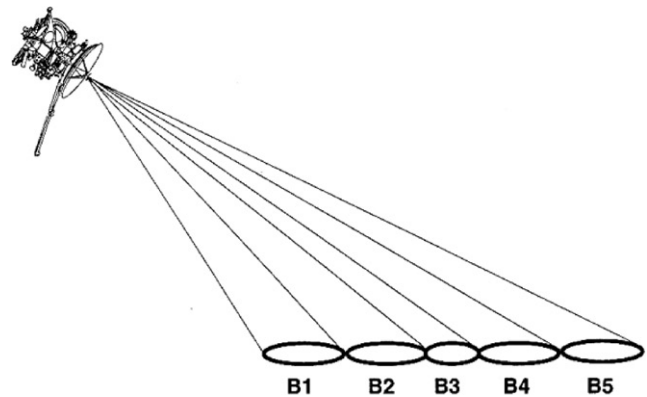


Fig. 3. During closest approach at altitudes of 4000 km or less, all 5 beams will be used to build an image swath. While the synthetic aperture imaging mode achieves high resolution through frequency-domain processing, radiometry data can also be obtained simultaneously. The radiometry will be confined to horizontal polarization (since the beams are aligned orthogonal to the polarization direction of the antenna) at incidence angles driven by the imaging requirements (typically $10\text{--}30^\circ$).

Within 10,000 km, altimeter observations may be more useful, and the spacecraft will be held nadir-pointing. Again, simultaneous radiometry will be performed. The simultaneous radiometry and altimetry will be of particular meteorological interest, since elevated terrain should be cooler by about 1 K/km due to the radiative-convective temperature profile of Titan's atmosphere (see later).

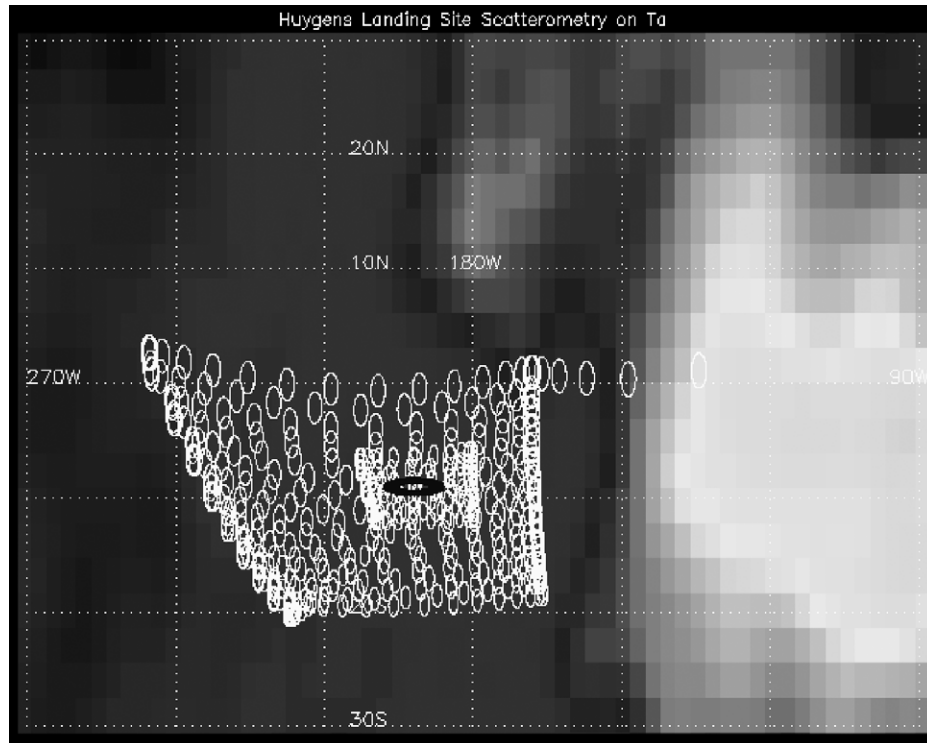


Fig. 4. Raster beam pattern. The observation shown here is the first one Cassini will make of Titan, on the inbound leg of flyby Ta. This raster, with individual beam footprints shown at 5 s intervals, is in fact for designed for scatterometry of the Huygens probe landing site (black ellipse), with incidence angles of only a few degrees. A second, smaller raster zooms in on the landing site from closer range, at a slightly different incidence angle. The background is a basemap made from Hubble Space Telescope images (see Smith et al., 1996) with the leading-face bright region on the right.

At 4000 km range, the spacecraft will turn to orient its 5 beams sideways for SAR imaging (Fig. 4). This will continue for about 20 min through closest approach until 4000 km range is exceeded outbound. Again, radiometry can be performed (through all 5 beams). As well as augmenting the interpretation of backscatter measurements, these radiometer observations will supplement the broader-coverage, but lower spatial resolution, measurements made during distant spirals. Because of the beam orientation, these radiometer measurements will be in H-polarization.

Outbound, the altimeter, scatterometer and radiometry spiral observations may be repeated in reverse order: now the spacecraft sees the antipode of the incoming observations (the Cassini spacecraft trajectory is only slightly bent by the Titan encounter).

Many Titan flybys are likely to be shared with other instruments, so isolated observations or combinations of the individual observations above may be performed on any given flyby. For example, an incoming asymptote on the day side of Titan might be devoted to optical remote sensing, while the closest approach and outgoing asymptote are devoted to RADAR. These plans are presently being formulated, and will doubtless change in any case after the first few encounters. At present, it is expected that SAR data will be taken on around 15–20 passes, cover-

ing about 20% of Titan's surface. As for radiometry, 4 half-passes are anticipated in the first year of the tour, starting with outbound-only radiometry on Ta in October 2004, with inbound radiometry on T4 in March 2005 and both in- and out-bound asymptotes devoted to radiometry on T8 in October 2005. Subsequent years of the tour are expected to include 6–8 half-passes of radiometry per year. Titan's surface will be essentially covered completely at some incidence and polarization, with some repeat coverage to look for seasonal change and exploit multiple incidence angles.

3. Titan

3.1. Titan surface observations

The earliest observations known to probe Titan's surface (as opposed to its atmosphere) were at microwave wavelengths. Jaffe et al. (1980) using the newly developed very large array (VLA) telescope, determined a microwave brightness at 6, 2, and 1.3 cm wavelength just prior to the Voyager 1 encounter (which measured the actual radius and temperature by radio occultation.) A microwave brightness temperature of around 87 K was reported, with an estimated radius of 2440 km.

A similar brightness temperature (86 ± 17 K at 3.5 cm; a weighted mean of all cm-wavelength data was 83.8 ± 6.4 K) was determined by Muhleman et al. (1990). This brightness temperature, assuming the surface temperature of 94 K and the known radius of 2575 km, corresponds to a microwave emissivity of around 0.85, and would be broadly consistent with a spherical body covered either in ice, or liquid or solid hydrocarbons.

It should be noted that the radar reflectivity of Titan (Muhleman et al., 1990) is substantially different from that of the Galilean satellites—see the discussion in Lorenz and Lunine (1997). In particular, the exceptionally high backscatter and polarization ratio for Europa, interpreted to be due to a coherent backscatter mechanism that relies upon scatterers distributed in relatively clean and cold (and therefore microwave-transparent) water ice, does not occur at Titan. Something is defeating this mechanism—perhaps impurities in the ice, and/or a low concentration of efficient scatterers.

More recently, near-infrared observations—both disk-integrated spectroscopy, and imaging using space telescopes (e.g. Smith et al., 1996), speckle imaging (Gibbard et al., 1999) and adaptive optics (e.g. Combes et al., 1998; Coustenis et al., 2001) have shown that Titan's surface is variegated, at least on scales down to the limiting resolution of ~ 300 km 'Bright' regions may be water ice plus other materials: 'Dark' regions are known (Gibbard et al., 1999) to have optical reflectivities of $< 5\%$, which is highly suggestive of hydrocarbon lakes. A mixed surface of 'ice' (which may include ammonia, rock and organics as well as water ice) and hydrocarbon lakes appears to be consistent with all the presently understood constraints.

3.2. Surface materials and dielectric properties

Titan's place in the solar system and its bulk density of 1880 kg m^{-3} suggest it is roughly 50% rock and 50% ice. Titan is large enough that accretional heating would have melted the ice component and allowed the bulk of the rocky material to sink to the center to form a rocky core (e.g. Stevenson, 1992). The outer layers and surface should be dominated by water ice and other volatiles. The latter almost certainly includes organic materials—perhaps surface reservoirs of methane and the products of methane photolysis, including ethane, acetylene and its polymers, other condensed organics, and the complex refractory photolysis product 'tholin' that appears to make much of the haze that obscures Titan's surface at optical wavelengths.

Another component that may be significant on Titan's surface is ammonia (Lorenz, 1998). Titan is likely to have incorporated much ammonia during its formation (principally as ammonia hydrates). Much of this material may have been photolysed rapidly into molecular nitrogen, some of which forms the bulk of the 1.5 bar atmosphere, some may be dissolved in ethane/methane surface liquids, and a

large amount may have been lost early in Titan's history, as suggested by the present-day nitrogen isotope ratios.

However, substantial amounts of ammonia may remain on Titan as a subsurface ocean or liquid mantle. The depression of the water freezing point by ammonia is significant—around 176 K. The water–ammonia peritectic composition at 176 K (approximately 30% ammonia) is the most likely composition for cryovolcanic flows, which may be superimposed on an ammonia-poor ice crust.

Late impact events, after a solid ice lithosphere formed, may have deposited some amounts of silicate or metallic material on Titan's surface, but the amount, geographical distribution and rate of subsequent burial of this material is completely unknown.

The dielectric properties of these materials are summarized in Table 1.

There are some particular points to note. First, because of the low liquid water content of these very cold materials, they are in general much more transparent to microwave radiation than terrestrial rocks and solid (with the exception of dessicated iron-poor desert sands and the very cold ice in central Greenland). This implies that much of the radiation that will be observed comes from several m or tens of m below the surface. The exceptions are ammonia-rich ice, and meteoric (silicate/iron) materials. Some polyacetylenes and nitriles are polar and could be absorbing in high concentrations (see, e.g. Thompson and Squyres, 1990) but are unlikely to be concentrated enough to be absorbing, although this is somewhat uncertain in the case of polyacetylenes.

The microwave absorptivity of ammonia-rich ice depends on the ammonia concentration and (strongly) on temperature. It is not yet clear whether ammonia-rich ice is absorbing because of the ammonia molecule itself (which has an inversion absorption at 35 GHz, the far wings of which may be responsible for the measured absorption at longer wavelengths) or because of thin conducting films of liquid that form at grain boundaries. The latter explanation seems somewhat more probable, since near-DC absorption has been shown to rise dramatically between 80 and 150 K (Lorenz and Shandera, 2001).

The second point to note is that the various classes of material differ in the real part of their dielectric constant. In particular, there are clear jumps between the values for liquid organics (1.6) to water ice (3.1) to ammonia-rich ice (4.5). These differences indicate promise that microwave observations may be able to discriminate between these different surface materials.

It may be noted that in ratio terms (usually the determinant factor for reflection and emission of electromagnetic radiation) the range of these dielectric constants is rather higher than is typical for dry terrestrial materials, although lower than the range between wet and dry terrestrial materials: land/sea contrasts will not be as high on Titan as on Earth, although they are well within the capabilities of the instrument.

Table 1
Physical properties of possible Titan surface materials at 94 K

Material	Dielectric constant	Loss tangent	Density (kg m ⁻³)	Thermal conductivity (Wm ⁻¹ K ⁻¹)	Likelihood	Comment
Water ice	3.12(G72)	2 × 10 ⁻⁵ (LT)	~900	~5@90 K (RK)	Major	LT 1.25 cm wavelength
Water-ammonia ice	4.5 (L98)	~0.01 (LS)	~900	1-2 (LS) 1.5@130 K (RK)	Major?	Loss tangent depends on ammonia concentration and temperature
Sludge	2.0–2.4	10 ⁻⁴ ?	~800?	0.5?	Major?	Mostly simple organics, but higher loss due to various alkynes and nitriles (TS) (Strongly depends on iron content)
Meteoritic material	8.6 (P92)	0.9	2700	2	Minor	
Methane clathrate	As ice?	As ice?	900	0.4 (Rk)	?	Tetrahydrofuran clathrate—methane clathrate similar
CO ₂ ice	2.2 (S80)	< 0.005 (S80)	~1600	1 (RK)	Possible	Thermal conductivity extrapolated
Lakes	1.8	10 ⁻⁵	650	0.25 ^a	Major?	weighted average of Ethane, Methane, Nitrogen
Ethane	1.95 (UL) 1.83 (TS) 1.9 (S92)	< 10 ⁻⁵ ? < 10 ⁻³ (S92)	650	0.27 ^a (B92)	Major	
Methane	1.71 (UL) 1.65 (TS)	< 10 ⁻⁵ ?	450	0.21 ^a (B92)	Major	
Nitrogen	1.51 (TS)	< 10 ⁻⁵ ?	800	0.2?	Minor	

Abbreviated references: B92 Birchley et al. (1992); G72 Gough (1972); L98 Lorenz (1998), LS Lorenz and Shandera (2001); LT Lamb and Turney (1949); M98 Maetzler (1998); P92 Picardi et al. (1992); RK Ross and Kargel (1998); S80 Simpson et al. (1980); S92 Sen et al. (1992); TS Thompson and Squyres (1990); UL Ulamec et al (1992).

^aNB liquid deposits are likely to be convective.

3.3. Thermal environment

The Voyager 1 Radio Occultation experiment (e.g. Von Eshleman et al., 1983) determined refractivity profiles of Titan's atmosphere down to the surface. The inversion of these profiles into temperature requires an assumed atmospheric composition. The two refractivity profiles were essentially identical; as expected the diurnal temperature changes in Titan's dense lower atmosphere were unmeasurably small. The two radio occultation points (6°N, 258°E and 8°S 76°E) did not differ significantly in latitude (Lindal et al., 1983).

McKay et al. (1997) re-analyze the radio occultation data with different assumptions regarding methane humidity: for plausible humidities near the surface of 0.6, lapse rates of 1–1.4 K/km are encountered in the lowest 4 km of the atmosphere.

4. Theory—thermal emission from a dielectric surface

Passive microwave measurements by themselves or in conjunction with radar measurements have proven valuable in determining thermophysical properties of planetary surfaces. Much of this early work was stimulated by efforts to understand the Moon, and fundamental techniques were developed decades ago to interpret lunar radio data

in terms of surface properties (Hagfors, 1970). Troitsky (1957) first advanced the idea that the effective dielectric constant of the Moon's surface could be determined from polarized microwave brightness measurements across the lunar disk. This was followed by a series of observations (Soboleva, 1962; Heiles and Drake, 1963, and others following) that culminated in a fairly complete description of the frequency-dependent dielectric constant of the lunar surface and its significance by the early 1970s (e.g. see White and Cogdell, 1973).

The basic approach is best understood with reference to a smooth dielectric sphere at a constant temperature as described by Heiles and Drake, the brightness distribution across which would display a unique polarized pattern that would allow the determination of its dielectric constant ϵ . For any portion of its surface viewed at an incidence angle θ , reflection coefficients R_v and R_h for the vertical and horizontal polarizations, respectively, are given by the Fresnel relations:

$$R_h(\theta) = \left| \frac{\cos \theta - \sqrt{\epsilon - \sin^2 \theta}}{\cos \theta + \sqrt{\epsilon - \sin^2 \theta}} \right|^2,$$

$$R_v(\theta) = \left| \frac{\epsilon \cos \theta - \sqrt{\epsilon - \sin^2 \theta}}{\epsilon \cos \theta + \sqrt{\epsilon - \sin^2 \theta}} \right|^2.$$

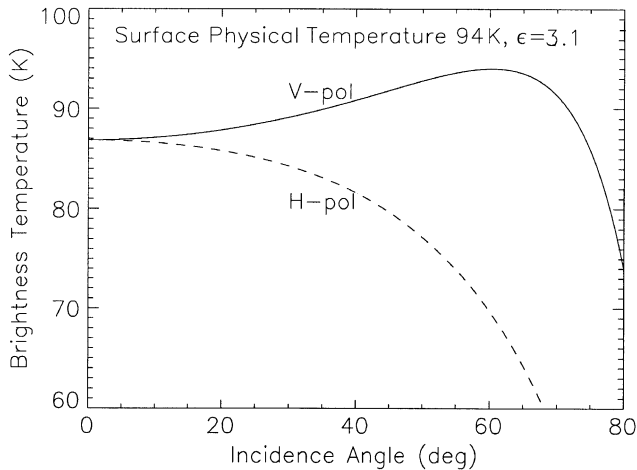


Fig. 5. Vertically and Horizontally polarized microwave brightness temperature for a smooth surface at 94 K. The vertically polarized radiation increases to a peak at the Brewster angle and then drops. The horizontally polarized radiation falls monotonically with angle: measured emission is fairly insensitive to polarization for small incidence angles.

The brightness temperature T_b sensed for polarization $p = (h \text{ or } v)$ is given by

$$T_b(\theta) = (1 - R_p(\theta))T_s,$$

where T_s is the physical or thermodynamic temperature of the surface.

Fig. 5 shows the brightness temperature in both polarizations as a function of incidence angle for pure ice ($\epsilon = 3.1$). The zero-incidence brightness temperatures are the same for both polarizations, and are slightly lower than the physical temperature because of the imperfect dielectric matching of the surface to free space. The horizontally polarized radiation decreases monotonically with incidence angle, while the vertically polarized brightness temperature rises slowly to a peak and then drops.

This peak occurs (i.e. R_v is zero) where θ has the value $\arctan(\epsilon^{0.5})$, the Brewster angle. At this angle, vertically polarized radiation is completely transmitted into or out of the material and no radiation is reflected. This phenomenon has been used to in bistatic radar scattering experiments on planetary surfaces, where a plot of scatter power against angle has a minimum (zero) at the Brewster angle, allowing the dielectric constant of the surface material to be estimated.

Here, a curve of brightness temperature has a maximum, equal to T_s , at the Brewster angle. This is of importance for two reasons. First is that the dielectric constant can be similarly estimated from a curve of measured brightness temperatures against incidence angle (although we note that in the presence of noise, it is easier to determine the peak of an emission as here, than to determine the minimum of reflectance—radiometry is therefore a more secure method of performing this analysis than is bistatic scattering). Second, by making measurements at or close to the Brewster

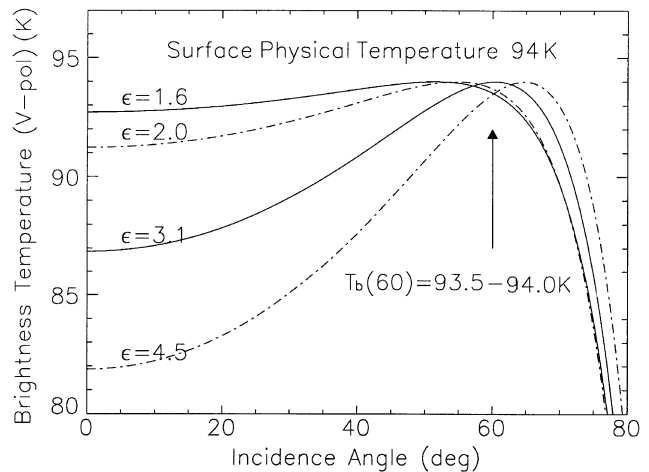


Fig. 6. Vertically polarized brightness temperature as a function of incidence angle and surface composition. The curves for different materials are quite distinct, and could be fit by observations at different incidence angles. Even without performing a full curve fit to determine the temperature at the Brewster angle, the surface temperature can be estimated with reasonable accuracy for the materials here by measuring at 60° .

angle, the brightness temperature can be straightforwardly interpreted as a physical surface temperature, independent of composition.

Fig. 6 shows the vertically polarized brightness temperature for a variety of surface materials (dielectric constants). It can be seen that the curves are quite distinct, allowing composition identification from measurements at several incidence angles—combining data from several looks at the same spot during spiral or mosaic scans could be performed, or a spot of specific interest could even be ‘spotlighted’ during a flyby, measuring a curve directly. Since the Brewster angles of the various materials lie in the range $51\text{--}65$ degrees, brightness temperatures at 60° incidence can be interpreted directly as a real surface temperature with only a 0.5 K error. If further observations are available (e.g. at other incidence angles) to constrain the dielectric constant, this error can be reduced significantly. Note that if the boresight of the beam intersects the surface at an angle θ , then the instrument will sense the sum of contributions from parts of the surface at a range of angles, roughly from $\theta - \phi$ to $\theta + \phi$ at the near- and far-ends of the footprint, where ϕ is the half-beamwidth. Also, if the boresight is aligned to be exactly vertically polarized, the left and right edges of the beam will not be exactly vertical, so there will be some H-pol contribution.

Another approach to data interpretation is to compare the brightness temperatures in the two polarizations.

As seen in Fig. 5, these diverge with incidence angle, so maximum contrast occurs at high incidence angles. There will be a tradeoff in that signal-to-noise will degrade and incidence angle uncertainties increase at higher incidence. We show in Fig. 7a ‘carpet’ plot of the two brightness temperatures at 50° degrees incidence, an achievable incidence

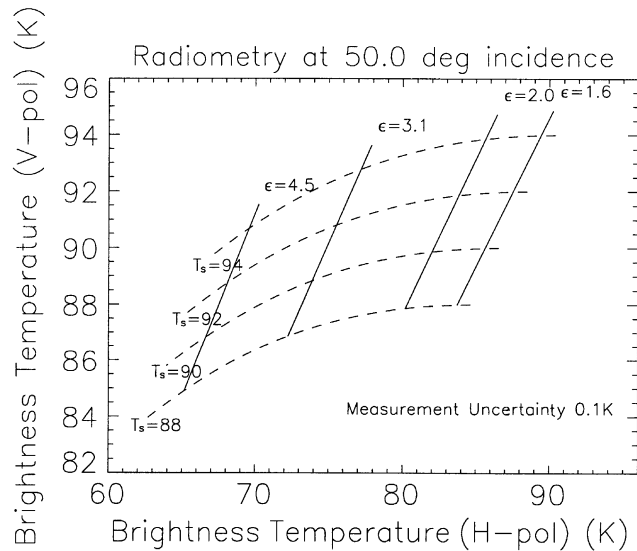


Fig. 7. Carpet plot—points defined by horizontal and vertical brightness temperatures at moderate incidence angles map directly to physical temperature and composition. The ellipse in the lower left shows a ± 0.1 K relative measurement uncertainty; absolute uncertainty is around 2 K.

angle (and approximately that used routinely by terrestrial radiometers and scatterometers). Measurements at both polarizations for a location on Titan's surface can be plotted on this chart and the dielectric constant of the surface, and its physical temperature, can be simply read off. The difference in horizontally polarized brightness temperature between different surface compositions is 1–2 orders of magnitude above the measurement uncertainty.

In practice departures from the idealized case of a smooth sphere must be accounted for; e.g., surface roughness and temperature variations among others. In the analysis of lunar observations it was noted that the consideration of percentage polarization $(T_{bv} - T_{bh}) / (T_{bv} + T_{bh})$ effectively made the interpretations independent of temperature effects. Surface roughness was a major effect—surface variations on scales much larger than the wavelength of measurement were accounted for by describing each measurement point as an appropriate average over an ensemble of planes whose local verticals are distributed in a cone around the nominal vertical. Shadowing was a related consideration important at large incidence angles. Observations over an otherwise uniform sphere could then be interpreted in terms of both the dielectric constant and a parameter describing the roughness; e.g., the standard deviation of the local vertical around the nominal. This approach was successfully used to determine a frequency-dependent lunar-average dielectric constant with a value that varied monotonically from 1.34 ± 0.04 at 3 mm wavelength (White and Cogdell, 1973) to 2.1 ± 0.3 at 21 cm (Heiles and Drake, 1963), with corresponding surface roughness standard deviation $\sim 20^\circ$ at short wavelengths to effectively zero at the longest wavelengths. The roughness variation was readily interpreted as

due to relative smoothing at longer wavelengths, but taken as a caution in the interpretation by White and Cogdell that scattering effects on the order of a wavelength become important at the shorter wavelengths. Such effects are more difficult to model and hence interpret. Regional variations in dielectric constant did not appear to be significant in the analyses.

Our approach for Titan will be based on this approach. Although we anticipate that there will be significant regional variations in surface parameters if both solid and liquid phases are present on the surface, we have a distinct advantage over lunar observations because we may tailor our scheme to observe a given location at different angles to determine its unique incident-angle polarization dependence.

As with the moon, large-scale surface roughness will be readily determined using this model. However, we have no knowledge of what the small-scale roughness might be and how this may affect the results. In this we include the case where the typical low loss tangent of low-temperature ices coupled with internal scattering of unknown but possibly significant magnitude leads to emittance properties quite unlike those encountered on the Moon. Such effects can lead to results that depart significantly from the lunar-based model. We expect that our challenge will be (1) to identify such anomalous regions, and (2) to combine the radiometer data with radar scattering and other relevant data to expand our model so that we may determine additional physically interesting parameters describing these regions. On the other hand, liquid regions with depths exceeding the penetration depth will present the most simple case for which a precise and unambiguous dielectric constant may be obtained.

5. Scientific observations by Cassini

In this section, we outline some specific science goals for Cassini and investigate how radiometry will address them.

5.1. Variation of temperature with latitude

Voyager infrared spectra have been re-analyzed (Samuelson et al., 1997) and confirm the earlier finding that shows a drop in brightness temperature with latitude at 530 cm^{-1} , a wavelength believed to sound the temperature of the atmosphere just above the surface. The inferred temperatures drop from about 93 K near the equator, to 89 K at around 60° latitude. It is possible that these brightness temperatures are influenced by stratospheric emission (where the temperature contrast is rather larger) and so the thermodynamic temperature on the contrast is small and consistent with pre-Voyager estimates of latitudinal temperature contrast (< 0.1 K), but it has been noted (Lorenz et al., 2001b) that the 4 K contrast is consistent with a principle of maximum entropy production (MEP) by latitudinal heat flow, a principle that appears to hold for the Earth and Mars.

Since the microwave brightness temperatures are not significantly affected by stratospheric emission, the Cassini radiometer observations we simulate in this paper should be easily able to discriminate between the 0.1 and 4 K temperature contrasts described above.

5.2. Altitude discrimination of surface features

Another important effect we hope to look for is variation of brightness with altitude, due to the radiative–convective temperature profile of Titan’s atmosphere. A dry adiabat near Titan’s surface is around 1.3 K/km; the moist adiabat for methane–nitrogen is around 0.6 K/km (e.g. McKay et al., 1997). Recently, Courtin and Kim (2002) found an anomalous region on Titan in analyses of Voyager infrared data—this feature, at around 35°N, 340°E has a 530 cm⁻¹ brightness temperature ~ 3 K cooler than comparable areas, suggesting that it is a low emissivity area, physically colder and/or elevated relative to the surrounding terrain, or was obscured by a cloud. Microwave radiometry measurements will be unaffected by clouds and are therefore well-poised to resolve this issue.

The simultaneous altimeter and radiometer observations will be of particular relevance here and (assuming a constant composition along the groundtrack) can be interpreted as relative temperature, noting that the incidence angle is zero. For example, during the Earth swingby—the cold, dry Andes lay on a dry adiabat, whereas Eastern South America followed a wet adiabat more closely (Lorenz et al., 2001a). Additional observations (either radiometry at off-nadir incidence angles or backscatter measurements) would be required to determine any composition differences.

5.3. Bulk composition of surface units

In addition to the light–dark variegation seen in Hubble Space Telescope and other images of Titan’s surface, there may be changes in surface cover with latitude. One explanation of the symmetric surface temperatures inferred from the Voyager IRIS data is that the polar temperatures are ‘pinned’ by a large liquid nitrogen–methane reservoir, a situation much like that on Mars, but with liquid polar ‘caps’ (Stevenson and Potter, 1986).

In addition to the pure temperature changes with altitude there may be additional effects. For example, higher terrain may receive more rainfall, perhaps washing the icy surface clear of dark organics to yield the bright regions seen by HST. Condensation phenomena like frosts are conceivable (although given our present understanding of methane–nitrogen thermodynamics, unlikely—see Lorenz and Lunine, 2002). Indeed, metallic tellurium frost has been inferred from microwave measurements of high-altitude regions on Venus (Tyler et al., 1991; Pettengill et al., 1992, 1996), although both backscatter and emission data led to this interpretation.

It should be noted that Brewster angle effects are more easily explored at Titan where materials have typical dielectric constants of 1.5–5, and therefore Brewster angles of 52–65°, whereas terrestrial rocks and soils have higher dielectric constants, and therefore Brewster angles that are higher, corresponding to near-grazing incidence and thus more susceptible to incidence angle uncertainty effects.

5.4. Detection of geothermal anomalies

Approximately, the penetration depth of microwave radiation into (and thus the depth sounded by passive radiometry) for icy/organic materials ($\epsilon \sim 2-4$) is $\sim \lambda / (10 \times \text{loss tangent})$, with λ the wavelength. Loss tangents of 10^{-4} – 10^{-5} seem to be typical for ice and organics at these low temperatures—see Table 1—(quite possibly because these are the lowest losses that can be reliably measured. Thus, the penetration depth for our 2 cm wavelength may be as high as 2–20 m. If the surface is ammonia-rich, the loss tangent may be higher and we may penetrate only a few cm, comparable with typical imaging radar penetration into rocks or soil on Earth.

Taking chondritic radiogenic heat production for Titan’s core and thermal conductivity of ice yields a subsurface temperature gradient of about 1–2 K/km. Thus, on a globally averaged basis, the subsurface temperature influence on brightness temperature should be below our detection threshold of ~ 0.1 K. Note, however, that the global average may be misleading. For example, the geothermal heat flow over the entire Yellowstone basin is about 20× the terrestrial average: a corresponding enhancement (perhaps with an attendant field of methane geysers, Lorenz (2002)) on Titan might be detectable, since the temperature gradient a could be 20–40 K/km, and thus detectably higher temperatures would be sounded by the radiometer.

5.5. Solid state greenhouse

There is the faint possibility of detecting diurnal subsurface temperature contrasts with microwave radiometry. Diurnal temperature contrasts are expected to be small, since the thick atmosphere will convect away solar heating deposited in a thin opaque surface layer.

However, if the surface layer is partly transparent to sunlight (specifically that red and near-infrared sunlight that reaches the surface, having been absorbed neither by methane nor the reddish haze) energy may be deposited deep enough in the surface not to be immediately convected away. The insolation spectrum comprises about 10% of the solar flux incident on the top of the atmosphere. At red and near-IR wavelengths, water ice has an absorption length of about 1 m. Thus, over a Titan day of $\sim 5 \times 10^5$ s, the temperature rise of a meter cube, assuming no loss to the atmosphere or by radiation, would be around 0.1 K.

The 10% number derives from radiative transfer models (McKay et al., 1989) tuned to fit visible albedo measurements. It is possible that there is some seasonal variation in this quantity—in particular the southern hemisphere may be rather clearer of haze during the Cassini mission (late southern summer) and thus diurnal insolation may be higher.

A positive observation places significant constraints on the surface constitution. No diurnal change will be observed if the surface is optically dirty and thus the sunlight is absorbed in the top few centimeters where it can be convected away, while in the unlikely case the surface is very transparent, the volume over which the sunlight is absorbed is too large to permit a significant temperature rise. Similarly, if the microwave penetration depth is too small or too large, the volume affected by the temperature rise will not be matched to that probed by the microwaves, and the heat pulse will be diluted into nondetection.

5.6. Depth estimation of lakes and seas

We will obtain some strips of radiometry when the spacecraft is performing SAR measurements, at $10\text{--}30^\circ$ incidence. These will have footprints of $5\text{--}50$ km, so we should obtain several resolution elements across features like crater lakes $300\text{--}500$ km across.

If we assume that with other data (from previous global spiral scans or mosaics) we can determine the composition of the bedrock (land) and of the liquid (assuming the center of the feature is deep enough that we only sense the liquid itself) then the radiometer data may be interpretable as lake-bottom topography.

The problem of a low-loss dielectric layer above a semi-infinite space is well-known in terrestrial remote sensing, for the measurement of lake ice—see for example Ulaby et al. (1986, p. 1598)—and is essentially a combination of two reflection coefficients taking into account the absorption in the layer.

The effect is most strongly seen in horizontally polarized radiation between about 40° and 70° incidence angle, when the transition from ‘shallow’ to ‘deep’ changes the brightness temperature by a little over 2 K. At nadir, or the low incidence ($10\text{--}30^\circ$) associated with near-Titan SAR and altimetry measurements when the beam footprint will be small, the change is about 1.5 K—certainly enough to be detected. However, the interpretation of the data this way may have too many uncertainties to be unique—the loss tangent of the liquid will be uncertain, the lake bottom is likely to be covered in sediments of uncertain composition and thickness, and bubbles or other scatterers in the liquid may also influence the brightness temperature at this level. However, radially symmetric geometries are likely to be highly suggestive of crater topography. For example, Fig. 8 shows a crude simulated profile of a crater with a submerged peak ring and a central peak: radiometer data show a detectable drop in brightness temperature over the submerged peak ring.

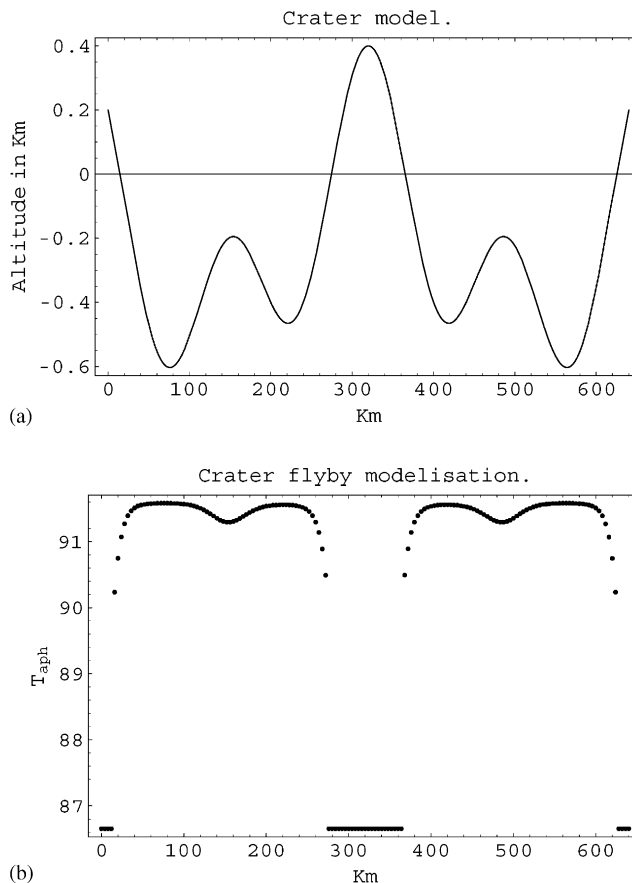


Fig. 8. (a) A topographic profile of a crater with a submerged peak ring and an exposed central peak. The horizontal line denotes the ‘sea level’—the rim and central peak are above the line and are assumed to be water ice at 94 K. (b) Simulated radiometer data show a detectable drop in brightness temperature over the submerged peak ring (assumed ice bedrock, $\epsilon = 3.1$, $\tan \delta = 1 \times 10^{-5}$; lake material $\epsilon = 1.88$ and $\tan \delta = 1 \times 10^{-5}$. Incidence angle = 10 degrees, typical for observations during SAR operations. There is a substantial drop in brightness temperature over exposed ice regions, namely the rim and central peak.

5.7. Microwave reflectivity from sun-glint

Although Cassini operates actively as a monostatic radar, there may be serendipitous opportunities to perform passive bistatic reflectivity measurements. On those occasions when radiometry mapping occurs on the dayside of Titan, the specular reflection of the sun may be detected by the radiometer. This effect was observed in a handful of isolated Magellan radiometer observations of Venus by Pettengill et al. (1992): the low altitude of Magellan, and the small beam footprint, meant that specular reflections were extremely rare. Cassini’s high altitude means there will be many opportunities for sunglint observations (with the optical instruments as well as with radar) and several dayside observations are planned with this in mind.

In the idealized case where Titan’s surface is a perfect (flat, 100% reflective) mirror, the sun reflection would add some 250 K to the observed brightness temperature,

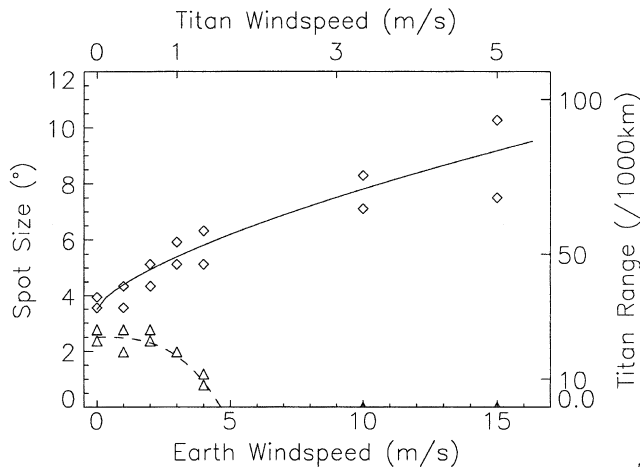


Fig. 9. Reflected solar brightness as a function of angle. The graph shows the size of the spot equal to 1/10 (dashed line, triangles) and 1/100 (solid line, diamonds) of the optical surface brightness of the sun at Earth as a function of sea-surface windspeed on Earth, from Strong and Ruff (1970) and Titan, assuming glint size relates to significant wave height and the windspeed-waveheight results of Ghafoor et al. (2000). The spot size ordinate refers to size in latitude and longitude extent—the corresponding range from Titan at which the radiometer beam has this size is shown at right.

assuming the typical solar microwave brightness temperature of 10,000 K and taking into account the beam dilution, since the sun has a diameter at Titan of only $\frac{1}{20}$ of a degree. Clearly, this reflection potentially presents some dynamic range problems (as indeed occurs on Earth, where microwave radiometers on meteorological satellites are routinely steered to avoid the reflection).

However, with realistic surface roughness, the absolute reflectivity falls to a fraction of unity, and the dynamic range required will be much lower. For example, optical data by Strong and Ruff (1970) shows that on ocean surfaces, the peak reflected radiance drops by a factor of 10 for windspeeds of only a few meters per second, or sea roughnesses corresponding to about 1 m/s winds on Titan (Ghafoor et al., 2000). The corresponding spot sizes are easily resolvable by the Cassini radiometer (see Fig. 9).

6. Conclusions

We have explored the application of the Cassini RADAR microwave radiometer to the investigation of Titan's surface, atmospheric transports and the near-surface interior. The microwave brightness measurements are completely unaffected by the atmosphere, whereas near- and far-infrared spectroscopy require the estimation and removal of significant atmospheric opacity and scattering. Even radio occultations to measure near-surface temperature rely on independent estimates of atmosphere composition.

While a single microwave brightness temperature measurement has a nonunique interpretation, we have shown

that a combination of looks at different polarization and incidence angle allows useful independent constraints to be placed on surface temperature and composition, addressing several key scientific goals.

Some outstanding issues require further modeling efforts to understand fully, such as the interpretation of radiometer data with incomplete polarization information (discussed briefly in Pettengill et al., 1992), and the exact choice of observation strategy. However, it is clear that the Cassini microwave radiometer is poised to make a significant contribution to our understanding of Titan.

Acknowledgements

The authors acknowledge the support of the Cassini project and CNRS. Athena Coustenis is thanked for a constructive and prompt review. An anonymous reviewer is thanked for a constructive review.

References

- Birchley, P.N.W., Daniell, P.M., Zarnecki, J.C., Parker, D.J., 1992. Laboratory determination of the thermal conductivity of liquid methane and ethane, in ESA SP-338. Proceedings of the Symposium on Titan, Toulouse, September 1991, pp. 311–314.
- Bolton, S.J., Janssen, M., Thorne, R., Levin, S., Klein, M., Gulkis, S., Bastian, T., Sault, R., Elachi, C., Hofstadter, M., Bunker, A., Dulk, G., Gudim, E., Hamilton, G., Johnson, W.T.K., Leblanc, Y., Liepack, O., McLeod, R., Roller, J., Roth, L., West, R., 2002. Ultra-relativistic electrons in Jupiter's radiation belts. *Nature* 415, 987–991.
- Combes, M., Vapillon, L., Gendron, E., Coustenis, A., Lai, O., Wittemberg, R., Sirdey, R., 1998. Spatially resolved images of Titan by means of adaptive optics. *Icarus* 129, 482–497.
- Courtin, R.D., Kim, S.J., 2002. Mapping of Titan's tropopause and surface temperatures from Voyager IRIS spectra. *Planet. Space Sci.* 50, 309–321.
- Coustenis, A., Gendron, E., Lai, O., Véran, J.-P., Woillez, J., Combes, M., Vapillon, L., Fusco, T., Mugnier, L., Rannou, P., 2001. Images of Titan at 1.3 and 1.6 μm with adaptive optics at the CFHT. *Icarus* 154, 501–515.
- Elachi, C., Im, E., Roth, L.E., Werner, C.L., 1991. Cassini Titan radar mapper. *Proc. IEEE* 79, 867–880.
- Elachi, C. et al., in press. RADAR: The Cassini Titan radar mapper, *Space Sci. Rev.*
- Eshleman, V.R., Lindal, G.F., Tyler, G.L., 1983. Is Titan wet or dry? *Science* 221, 53–55.
- Ghafoor, N.A.-L., Zarnecki, J.C., Challenor, P., Srokosz, M.A., 2000. Wind-driven surface waves on Titan. *J. Geophys. Res.* 105, 12,077–12,091.
- Gibbard, S.G., Macintosh, B., Gavel, D., Max, C.E., de Pater, I., Ghez, A.M., Young, E.F., McKay, C.P., 1999. Titan: high-resolution speckle images from the Keck Telescope. *Icarus* 139, 189–201.
- Gough, S.R., 1972. A low-temperature dielectric cell and the permittivity of hexagonal ice to 2 K. *Canad. J. Chem.* 50, 3046–3051.
- Hagfors, T., 1970. Remote probing of the moon by infrared and microwave emissions and by radar. *Radio Sci.* 5, 189–227.
- Heiles, C.E., Drake, F.D., 1963. The polarization and intensity of thermal radiation from a planetary surface. *Icarus* 2, 281–292.
- Ivanov, A.B., Muhleman, D.O., Vasavada, A.R., 1998. *Icarus* 133, 163–178.

- Jaffe, W., Caldwell, J., Owen, T., 1980. Radius and brightness temperature observations of Titan at centimeter wavelengths by the very large array. *Astrophys. J.* 242, 806–811.
- Janssen, M.A. (Ed.), 1993. *Atmospheric Remote Sensing by Microwave Radiometry*. Wiley, New York, 572pp.
- Johnson, J.R., Baker, V.R., 1994. Surface property variations in Venusian fluidized ejecta blanket craters. *Icarus* 110, 33–70.
- Lamb, J., Turney, A., 1949. Electrical properties of ice at 1.25 cm wavelength. *Proc. Phys. Soc. (London) B* 62, 272–273.
- Lindal, G.F., Wood, G.E., Hotz, H.B., Sweetnam, D.N., Eshleman, V.R., Tyler, G.L., 1983. The atmosphere of Titan—an analysis of the Voyager 1 radio occultation measurements. *Icarus* 53, 348–363.
- Lorenz, R., 1998. Preliminary measurements of the cryogenic dielectric properties of water–ammonia ices: implications for radar observations of icy satellites. *Icarus* 136, 344–348.
- Lorenz, R.D., 2002. Thermodynamics of geysers: application to Titan. *Icarus* 156, 176–183.
- Lorenz, R.D., Lunine, J.I., 1997. Titan's surface reviewed: the nature of bright and dark terrain. *Planet. Space Sci.* 45, 981–992.
- Lorenz, R.D., Lunine, J.I., 2002. Titan's snowline. *Icarus* 158, 557–559.
- Lorenz, R., Shandera, S., 2001. Physical properties of ammonia-rich ice: application to Titan. *Geophys. Res. Lett.* 28, 215–218.
- Lorenz, R.D., Elachi, C., West, R.D., Johnson, W.T.K., Janssen, M.A., Moghaddam, M., Hamilton, G., Liepack, O., Bunker, A., Roth, L.E., Wall, S.D., Dente, L., Casarano, D., Posa, F., 2001a. *J. Geophys. Res.* 106, 30,271–30,280.
- Lorenz, R., Lunine, J.I., Withers, P.G., McKay, C.P., 2001b. Titan, Mars and Earth: entropy production by latitudinal heat flow. *Geophys. Res. Lett.* 28, 415–418.
- Maetzler, C., 1998. Microwave properties of ice and snow, In: Schmitt, B., et al. (Eds.), *Solar System Ices*. Kluwer, Dordrecht.
- McKay, C.P., Martin, S.C., Griffith, C.A., Keller, R.M., 1997. Temperature lapse rate and methane in Titan's troposphere. *Icarus* 129, 498–505.
- McKay, C.P., Pollack, J.B., Courtin, R., 1989. The thermal structure of Titan's atmosphere. *Icarus* 80, 23–53.
- Melacci, P.T., Orosei, R., Picardi, G., Seu, R., 1998. Cassini radar: system concept and simulation results. *Planetary and Space Science* 46, 1363–1374.
- Muhleman, D.O., Grossman, A.W., Butler, B.J., Slade, M.A., 1990. Radar reflectivity of Titan. *Science* 248, 975–980.
- Pettengill, G.H., Ford, P.G., Wilt, R.J., 1992. Venus surface radiothermal emission as observed by Magellan. *J. Geophys. Res.* 97, 13,091–13,102.
- Pettengill, G.H., Ford, P.G., Simpson, R.A., 1996. Electrical properties of the Venus surface from bistatic radar observations. *Science* 272, 1628–1631.
- Picardi, G., Seu, R., Coradini, A., Zampolini, E., Ciaffone, A., 1992. The radar system for the exploration of Titan, II. *Nuovo Cimento (C)* 15, 1149–1161.
- Ross, R.G., Kargel, J.S., 1998. Thermal conductivity of ices, In: Schmitt, B., et al. (Eds.), *Solar System Ices*. Kluwer, Dordrecht.
- Samuelson, R.E., Nath, N.R., Borysow, A., 1997. Gaseous abundances and methane supersaturation in Titan's troposphere. *Planet. Space Sci.* 45, 959–980.
- Sen, A.D., Anicich, V.G., Arakelian, T., 1992. Dielectric constant of liquid alkanes and hydrocarbon mixtures. *J. Phys. D.* 25, 516–521.
- Simpson, R.A., Fair, B.C., Howard, H.T., 1980. Microwave properties of solid CO₂. *J. Geophys. Res.* 85, 5481–5484.
- Skou, N., 1989. *Microwave Radiometer Systems: Design and Analysis*. Artech House, Norwood MA, 163pp.
- Smith, P.H., Lemmon, M.T., Lorenz, R.D., Caldwell, J.J., Allison, M.D., Sromovsky, L.A., 1996. Titan's surface revealed by HST imaging. *Icarus* 119, 336–349.
- Soboleva, N.S., 1962. Polarization measurement of the moon radio emission with the aid of a big Pulkovo radio telescope at a wavelength of 3.2 cm. *Astron. Zh.* 39, 1124–1126.
- Stevenson, D.J., 1992. The interior of Titan, in ESA SP-338. *Proceedings of the Symposium on Titan, Toulouse, September 1991*, pp. 29–33.
- Stevenson, D.J., Potter, A.E., 1986. Titan's latitudinal temperature distribution and seasonal cycle. *Geophys. Res. Lett.* 13, 93–96.
- Strong, A.E., Ruff, I.S., 1970. Utilizing satellite-observed solar reflections from the sea surface as an indicator of surface wind speeds. *Remote Sensing Environ.* 1, 181–185.
- Thompson, W.R., Squyres, S.W., 1990. Titan and other icy satellites—dielectric properties of constituent materials and implications for radar sounding. *Icarus* 86, 336–354.
- Troitsky, V.S., 1957. To the theory of the moon radio emission. *Astron. Zh.* 31, 511–521.
- Tyler, G.L., Ford, P.G., Campbell, D.B., Elachi, C., Pettengill, G.H., Simpson, R.A., 1991. Magellan—electrical and physical properties of Venus' surface. *Science* 252, 265–270.
- Ulaby, F.W., Moore, R.K., Fung, A.F. (Eds.), 1986. *Microwave Remote Sensing, Vols. I & III*. Artech House, Norwood, MA.
- Ullamec, S., Badoz, J., Lebreton, J.-P., 1992. Dielectric constant measurements in simulated Titan ocean liquids, in ESA SP-338. *Proceedings of the Symposium on Titan, Toulouse, September 1991*, pp. 401–405.
- White, T.L., Cogdell, J.R., 1973. Lunar polarization studies at 3.1-mm wavelength. *Moon* 6, 235–249.